Marine and Petroleum Geology 179 (2025) 107450

Contents lists available at ScienceDirect

Marine and Petroleum Geology

journal homepage: www.elsevier.com/locate/marpetgeo

Optimizing CO_2 hydrate storage and avoiding leakage: Numerical analysis of the self-restoring formation process of hydrate caps in submarine sandy silts

Mengyang Li [a], Shuanshi Fan [a,b,*], Yanhong Wang [a], Xuemei Lang [a,b], Gang Li [a]

[a] School of Chemistry and Chemical Engineering, South China University of Technology, Guangzhou, 510640, China
[b] Key Laboratory of Fuel Cell Technology of Guangdong Province, Guangzhou, 510640, China

ARTICLE INFO

Keywords:
Carbon capture and storage
CO_2 hydrate
Sandy silt
Sealing cap
Parameter optimization
Reservoir simulation

ABSTRACT

The sequestration of CO_2 in the form of hydrate within submarine sediments represents a promising strategy in Carbon Capture and Storage (CCS). However, the internal mechanisms governing CO_2 hydrate formation in sandy silty strata remain unclear. This paper established a multi-field coupled numerical model to simulate the formation process of CO_2 hydrate cap in a sandy silty layer in medium-depth seawater depth in the South China Sea for the first time and to evaluate the effects of different formation and injection parameters on the sealing capacity and leakage capacity. The results show that the optimum formation parameters are an initial permeability of 100mD and water saturation of 0.3. The porosity has the least effect on the sealed storage in the range of 0.2–0.4. The pressure of the injection well is slightly higher than the formation pressure and the temperature is close to the phase equilibrium temperature to achieve the ideal sealing effect. The region with high liquid CO_2 saturation shows horizontal diffusion between 200 and 400m. In addition, the high-pressure zone extended approximately 150m from the wellhead, with the final temperature diffusion matching the injection well up to about 20m from the wellhead. In the range of 150-400mbsf, a higher injection well location forms a broader lateral hydrate cap and a wider liquid CO_2 seepage range. This study provides theoretical guidance for selecting suitable formations and ensuring effective leakage control of specific sandy silty strata in the South China Sea at medium depth.

1. Introduction

Carbon dioxide (CO_2) capture and storage (CCS) is widely recognized as a key technology for mitigating adverse climate change (Ali et al., 2022; Zhao et al., 2024), providing low-carbon fuel and electricity (Bistline and Blanford, 2021), decarbonizing industrial processes, and facilitating the removal of CO_2 from the atmosphere (Bui et al., 2018; Krevor et al., 2023; Yu et al., 2021). An accurate understanding of potential capture and storage mechanisms is essential for the successful implementation of a safe, reliable, and widely accepted CCS program (Matter et al., 2016; Tyne et al., 2021).

Gas hydrate is formed by methane, CO_2, and other gases dissolved in water at high pressure and low temperature (Sloan, 2003; Sun et al., 2024b). It has a strong gas storage capacity (1 volume of hydrate can store 180 vol of gas) and a large storage potential (the stored fuel is 2–3 times that of the fossil energy that has been discovered) (Yu et al., 2021). CO_2 sequestration in the form of hydrates within submarine sediments presents a unique CCS strategy with several advantages over traditional geological sequestration methods. First, the main capture mechanisms of terrestrial sequestration, such as residual capture (Ajayi et al., 2019), dissolution capture (Li et al., 2023b), and mineral capture (Fu et al., 2023; Kalam et al., 2021; Snæbjörnsdóttir et al., 2020) are also applicable in this context (Khandoozi et al., 2023). Secondly, in most Marine sediments, pore fluid closely resembles seawater, meaning that the replacement of pore fluid during CO_2 storage poses minimal environmental risks. However, for terrestrial storage, the pore fluids typically exhibit higher salinity and may contain toxic metals, such as lead and arsenic, due to geological processes like evaporation and the hydrological cycle (Schrag, 2009). The third advantage is the abundance of pore space and the loose skeletal structure of seafloor sediments, which negates the need for complex drilling techniques, thus reducing both costs and the risk of CO_2 leakage (Ali Hussein et al., 2023). The fourth point is

* Corresponding author. School of Chemistry and Chemical Engineering, South China University of Technology, Guangzhou, 510640, China
E-mail address: ssfan@scut.edu.cn (S. Fan).

https://doi.org/10.1016/j.marpetgeo.2025.107450
Received 11 December 2024; Received in revised form 23 April 2025; Accepted 29 April 2025
Available online 30 April 2025

that the formation of the CO_2 hydrate cap can also protect the geological stability of the depleted methane hydrate zone and store a large amount of CO_2(Sambo and Gupta, 2025; Sun et al., 2019). Compared with the direct depressurized exploitation of gas hydrate, the CO_2 hydrate cap increased gas production by 146.56 % and decreased water production by 37.47 % (Guo et al., 2024). Finally, an effective containment barrier can be established by combining the negative buoyancy zone (NBZ) and the hydrate formation zone (HFZ) within the sediment (Li et al., 2022c). This storage barrier significantly differs from the issues of ocean acidification and marine ecosystem damage associated with the direct storage of seawater (Hofmann and Schellnhuber, 2010).

Research on CO_2 storage through the hydrate method has made preliminary progress (Bhati et al., 2025). In terms of the prevention of CO_2 leakage, Li et al. (2022c) assumed the occurrence of CO_2 leakage, through experimental simulation, and found that as CO_2 hydrate gradually forms in sediments, it obstructs the migration of leaked CO_2 to the seabed. This results in a gradual reduction in CO_2 injection from the seabed. The formation of a hydrate cap with appropriate high saturation in the sediments above the leakage point facilitates secondary storage of CO_2. Qanbari et al. (2011) reported that CO_2 emissions from power plants injected at depths of approximately 800m below the seabed will rise until a depth of about 360m below the seabed, at which point CO_2 forms a hydrate cap layer, preventing further upward migration. CO_2 can migrate an additional 135m before reaching the negative buoyancy zone. Teng and Zhang (Teng and Zhang, 2018) observed low buoyancy and high viscosity slow the formation of rising plumes, while the formation of hydrate sealing layers effectively reduces permeability, ensuring the safe and permanent sequestration of CO_2 in marine sediments. Zhao et al. (2023) found that the strength of hydrate cover increases as hydrate formation continues. When hydrate saturation falls below 27.8 %, the hydrate cap becomes unstable, and liquid CO_2 may break through, leading to leakage.

During the storage process, the formation of CO_2 hydrate affects the multiphase flow of liquid CO_2 and water within porous media. In this regard, Yamada et al. (2024) proposes a new method for hydrate risk assessment in the CO_2 process based on machine learning. Nakashima and Sato (Nakashima and Sato, 2016) discovered that hydrate primarily forms at the leading edge of gas fluid. After the gas front passes, significant hydrate formation occurs in the sediment. Whether the gas flow is obstructed depends on the remaining water saturation of the water in front of the gas and the formation rate under specific temperature and pressure conditions. Yu and Uchida (Yu and Uchida, 2020) highlighted the importance of the injection conditions and hydrating formation rates for the storage of CO_2 in seafloor sediments. Their study revealed that vertical extension strain near the well immediately follows fluid injection due to the increase in pore pressure. However, the strain gradually decreases as CO_2 hydrate forms. Sawano et al. (2022) provided a numerical model to simulate hydrate formation in the presence of CO_2-water two-phase flow in microscopic sand and stone pores. The simulation results show that at low hydrate saturations, particle-coated hydrates form more readily, while the injection flow rate has minimal impact on the permeability reduction. As hydrate growth progresses and most of the water converts to hydrate, the effect of flow rate on permeability becomes more pronounced. At high flow rates, water removes additional water from the surface of the sand and deposits it behind the sand grains, creating more pores to be filled by the hydrate. Liu et al. (2023) investigated the feasibility and storage capacity of CO_2 storage in the mined hydrate reservoirs. Their findings suggest that increasing reservoir pore volume and reducing hydrate plugging can significantly enhance storage capacity. In addition, hydraulic fracturing can partially mitigate the impact of hydrate plugging around the wellbore, increasing gas storage volume. Almenningen et al. (2018) analyzed hydrate growth at the pore level through direct imaging of pore space in micromodel chips. High-field MR Imaging was employed to visualize the flow of CO_2 water drainage and hydrate formation, confirming significant hydrate growth when liquid CO_2 was injected into sandstone filled with unsaturated water. CO_2 hydrates can grow at the phase interface or in dissolved water. Sun et al. (2024a) found that the hydrate cap layer mainly expands along the flow direction and is significantly affected by the CO_2 phase state, operating pressure, and flow rate. Higher flow rates and pressures accelerate hydrate formation, which reduces the risk of injection well clogging and improves cap stability.

To sum up, the storage of CO_2 hydrate in submarine sediments involves the redistribution of liquid CO_2 and seawater after CO_2 enters the sediments, as well as the growth of hydrate at the CO_2-H_2O interface (Chen et al., 2024). However, systematic research on the formation of hydrate by liquid CO_2 is still lacking (Agrawal et al., 2023), particularly regarding the formation of solid hydrate in unenclosed submarine sediments (Chen et al., 2024). Although preliminary studies have explored CO_2 sequestration in the form of hydrate (Yang et al., 2024), the internal mechanism of closed cap formation in sandy silty strata remains unclear. Key questions include whether leakage occurs during storage, the extent of any potential leakage, whether leakage can be mitigated or even halted through the formation of a hydrate cover, and whether CO_2 can be permanently stored. Additionally, the regulation of hydrate formation kinetics within sediment layers needs further investigation (Dhamu et al., 2023), particularly the nucleation and growth of hydrate in porous media under temperature and pressure gradients at specific injection temperatures of CO_2 (Li et al., 2022a; Liu et al., 2024a). The formation of a hydrate cover layer alters the pore structure, affecting CO_2 transport. Finally, the effect of changes in reservoir porosity and permeability of the reservoir on the final CO_2 sealing volume and sealing stock is unclear.

Therefore, a multi-physical coupled modeling framework tailored to the marine geological sequestration of CO_2 in hydrate form is required to study the internal mechanisms of closed cap formation. This framework will help determine the optimal formation parameters and injection conditions for maximizing storage and ensuring minimal CO_2 leakage or effective leakage control.

Numerical Method

2. Numerical Method

2.1. Theoretical model

The finite element numerical method has been proven reliable in hydrate research (Wang et al., 2023; Wei et al., 2022). This study developed a large-scale numerical simulator using COMSOL Multiphysics. We developed the mathematical model using the multiphase flow control equation, the hydrate nucleation growth kinetic reaction equation, and the energy conservation equation.

2.1.1. Multiphase flow control equation

The mass balance and momentum equations for the two-phase displacement process in porous media can be expressed as follows:

$$\frac{\partial}{\partial t}(\phi\rho_i S_i) + \nabla\cdot(\rho_i u_i) = \dot{m}_i\ , i = c, w \tag{1}$$

$$u_i = -\frac{\kappa k_n}{\mu_i}(\nabla p_i - \rho_i g), i = c, w \tag{2}$$

In the above formulae, Φ is the porosity, S_i is the saturation of component i, ρ_i is the density of component i, u_i is the speed of component i, κ is the intrinsic permeability tensor, k_{ri} is the relative permeability of component i, μ_i is the dynamic viscosity of component i, p_i is the fluid pressure, and $\dot{m}_i$ is the local mass rate generated per unit volume of hydrate formation. The subscripts 'c' and 'w' refer to liquid CO_2 and seawater, respectively.

For liquid CO_2 with a density of 9–20 MPa and a temperature of 274–303 K, the procedure of Sawano et al. (2022) was adopted. Fitting

the polynomial for easy numerical simulation calculation:

$$\rho_c(T,P) \approx \sum_{i=1}^{4}\left(\sum_{j=1}^{4} a_{ij} T^{j-1}\right) P^{i-1} \tag{3}$$

Since the velocity u of the CO_2 hydrate phase is zero, the mass preservation equation of CO_2 hydrate formation can be written as:

$$\frac{d}{dt}(\phi \rho_h S_h) = -\dot{m}_h \tag{4}$$

In the above formula, $\dot{m}_h$ represents the local mass rate of hydrate formation per unit volume, while the subscript 'h' refers to the hydrate phase. The hydrate stoichiometry relates the hydrate formation rate to the consumption of CO_2 and water as follows:

$$\dot{m}_h = \dot{m}_c \frac{N_h M_w + M_c}{M_c} \tag{5}$$

$$\dot{m}_w = \dot{m}_c \frac{N_h M_w}{M_c} \tag{6}$$

M_w and M_c are the molecular weights of water and CO_2, respectively. Each stage's saturation follows the following relationship:

$$S_c + S_w + S_h + S_g = 1 \tag{7}$$

In the above formula, S_g is the free gas saturation in the sediment. The sum of the initial water saturation is 1; that is, $S_{w0} + S_g = 1$. Free gas is not involved in the hydrate reaction or displacement process. We used the Van Genuchten-Mualem (VGM) model to describe each phase's relative permeability in a three-phase CO_2-seawater hydrate displacement formation system (Chen et al., 1999).

$$k_{rw} = S_e^{\eta}\left[1 - \left(1 - S_e^{\frac{1}{m}}\right)^{m}\right]^2 \tag{8}$$

$$k_{rc} = (1 - S_e)^{\eta}\left(1 - S_e^{\frac{1}{m}}\right)^{2m} \tag{9}$$

The model shows the following correlation between effective saturation and P_C:

$$S_e = \frac{1}{[1 + (\alpha p_C)^n]^m} \tag{10}$$

Capillary pressure distinguishes the injection and non-injection stages. This relationship is described as follows:

$$p_C = p_c - p_w \tag{11}$$

2.1.2. Hydrate nucleation growth and formation model

The dynamic formation process of hydrate cap can be divided into four stages:(a) fluid injection-migration-diffusion; (b) formation of local hydrates; (c) local area blockage; The plugging range gradually expands until a zero permeable hydrate cap is formed (d) The formation of a hydrate cap (Yang et al., 2024). To describe this process, it is necessary to accurately describe the hydrate nucleation growth equation in the numerical simulation. The formation of hydrate nuclei is a random process. The classical nucleation theory (CNT) has been shown to accurately predict the position of the hydrate nucleus using numerical simulation (Fukumoto et al., 2018). The Arrhenius equation (Ke et al., 2019) defines the nucleation rate J in CNT as the number of nuclei formed per unit volume per unit of time:

$$J = A \cdot \exp\left(-\frac{\Delta\Psi^*}{k_B T}\right) \tag{12}$$

In the above formula, A is a pre-exponential factor or reaction frequency with a possible value of $0.2 \times 10^{-4}\ s^{-1}$ (Wei and Nobuo, 2023). k_B is the Boltzmann constant. $\Delta\Psi^*$ is the nucleation barrier for forming critical nuclei. We previously investigated the effects of temperature gradient, wall curvature, and roughness on the hydrate nucleation barrier (Li et al., 2022a, 2022b, 2023a). Our previous study (Li et al., 2024) determined that the $\Delta\Psi^*$ of homogeneous CO_2 hydrate nucleated with a sphere can be obtained as 1.92×10^{-19} J.

Micro-scale scale induction time t_{mic} can be expressed by nucleation rate J as follows (Yuhara et al., 2015):

$$t_{mic} = \frac{1}{JV_{mic}} \tag{13}$$

In the above formula, V_{mic} is the nuclei volume on a micro-scale. Similarity criteria can be used to estimate the site-scale induction time t for marine carbon sequestration:

$$\frac{t}{t_{mic}} = \frac{r}{r_{cc}} = \eta \tag{14}$$

r represents the effective radius for site-scale numerical simulation. r_{cc} is the critical radius for the nucleation of CO_2 hydrate at the micro-scale, while η is the amplification factor. Formulae (13-14) can then be used to calculate the induction time for site-scale nucleation as follows:

$$t = \frac{\eta}{JV_{mic}} \tag{15}$$

The Kim-Bishnoi model (Clarke and Bishnoi, 2005)can describe the rate function of CO_2 consumption due to hydrate formation as follows:

$$\dot{m}_c = k_f \cdot A_s\left(f_c - f_{eq}\right) \tag{16}$$

In the above formulae, k_f is the formation constant, A_s is the surface area of the porous medium involved in the reaction, f_c is the fugacity of CO_2 under the corresponding pressure P_c, and f_{eq} is the fugacity at equilibrium at temperature T and equilibrium pressure P_{eq}. The classical Chen-Guo model (Chen and Guo, 1998) is used in this study to calculate f_c and f_{eq}.

Formula 17 calculates the macroscopic and microscopic particle volumes of hydrate.

$$V = \frac{4}{3}\pi r^3 \tag{17a}$$

$$V_{mic} = \frac{4}{3}\pi {r_{cc}}^3 \tag{17b}$$

We can assume that the number of voids (N_V) for a macroscale hydrate particle volume V equals the number of solid particles, and the corresponding voids (V_V) can be calculated as follows:

$$V_V = \frac{\phi}{N_V} \tag{18}$$

$$N_V = \frac{(1-\phi)}{V_p} \tag{19}$$

The surface area of the hydrate formation reaction region can be expressed as follows:

$$A_s = N_V\left(4\pi r^2\right) S_h^{2/3} \tag{20}$$

At the microscopic scale, the critical CO_2 nucleation radius r_{cc} is 1.54 nm (Li et al., 2024). The Kozeny-Carman equation estimates the effective radius r of macro-scale hydrate particles as follows:

$$r = \left[45\kappa_0 \frac{(1-\phi)^2}{\phi^3}\right]^{1/2} \tag{21}$$

κ_0 is the inherent permeability of porous media. Hydrate formation in a porous brine aquifer reduces its porosity and permeability. The permeability change was calculated using the Masuda model (Masuda et al., 1999).

$$\kappa = \kappa_0 \cdot (1 - S_h)^n, n = 10, 15 \tag{22}$$

2.1.3. Thermal field control equation

Hydrate formation is an exothermic process that influences the temperature distribution during hydrate formation. Therefore, we must use the thermal energy balance equation to describe the temperature field change during hydrate formation. We can write the heat-energy balance equation as follows:

$$\left[\sum_i \phi\rho_i S_i C_i + (1-\phi)\rho_s C_{ps}\right]\frac{\partial T}{\partial t} + (\rho_c u_c C_c + \rho_w u_w C_w)\cdot\nabla T - \phi\rho_c S_c \sigma_c \frac{\partial p_c}{\partial t} - \rho_c u_c \sigma_c \cdot \nabla p_c = \nabla\cdot(\lambda\nabla T) + \dot{m}_h \Delta H_h, i = c, w, h \tag{23}$$

In the above formula, H_i is the enthalpy of phase i, T is the local temperature of the system region, λ represents the thermal conductivity of the hydrate-bearing medium, and q indicates the surrounding heat resources. The subscript 's' indicates the sandy silt phase. ΔH_h is the enthalpy change of hydrate formation. σ represents the Joule-Thomson coefficient of the system phase due to the Joule-Thomson effect we studied (Castaneda et al., 2025).

2.2. Initial and boundary conditions

The pressure distribution within seafloor sediments is proportional to hydrostatic pressure. The empirical formula for hydrostatic pressure is given below:

$$P_{pw} = P_{atm} + \rho_w g(h + z) \tag{24}$$

In the above formula, P_{atm} is the atmospheric pressure at 0.101325 MPa, ρ_w is the water's density, g is gravity's acceleration, and h and z are the sediment and seawater depths, respectively.

The reservoir's temperature distribution is determined by the following equation that considers both the seafloor temperature and geothermal gradient:

$$T = T_{sf} + gradT \cdot h \tag{25}$$

In the above formula, T_{sf} is the seafloor temperature, and grad T is the geothermal gradient,which is 0.04 °C/m. We set the seawater layer's temperature to 2 °C.

The Dirichlet boundary condition determines the reservoir model's boundary while keeping the constant temperature and pressure values. Fig. 1(A) shows the schematic diagram of the model. The size of the model is 800 m × 500 m. The top of the model is a seawater layer with a water depth of 1200m. The middle is a hydrate cambium with a depth of 150m, and the lower layer is a CO_2 injection well area with a thickness of 250m. Fig. 1(B) depicts the initial distribution of pressure and temperature in the reservoir. The top is a marine layer (ML), the middle is a hydrate formation layer (HFL), and the bottom is a CO_2 injection layer (IL). The marine layer is simulated as a pseudo-porous medium, with porosity set to 1 and permeability set to 5.0 × 10^{-9} m^2. Table 1 shows the parameters used in the simulation.

2.3. Model verification

There is no publicly available data on the implementation of the South China Sea CO_2 storage project (Xia et al., 2024). To verify the accuracy of the simulation, we compared the developed model with the small-scale experiment implemented by Inui et al. (2011) as shown in Fig. 2(A) and considered by Yu et al. (2016) to be suitable for numerical simulation, as shown in Fig. 2(B). The results obtained in Fig. 2(B–C) show that there is a gap between the numerical simulation and the actual experiment in simulating temperature drops, and the accuracy of the simulation needs to be improved. In short, the simulation results of the model proposed in this work as shown in Fig. 2(C) can reproduce the experimental results and can be applied to the research of the actual site scale.

3. Results and discussion

3.1. Dynamic evolution law of hydrate formation process

The study of the dynamic evolution of hydrate saturation, CO_2 saturation, formation temperature, and formation pressure during the

Table 1
Parameters of mid-depth sandy silty formation in the South China Sea for simulation.

symbol	Value	Description
η_n	3.95 × 10^{-5} Pa s	Dynamic viscosity of CO_2
ρ_w	1045 kg/m^3	Sea water density
η_w	2.54 × 10^{-4} Pa s	Hydrodynamic viscosity
K_f	2.59 × 10^{-13} kg/Pa•s•m^2	Kinetic constant
ρ_h	1117 kg/m^3	CO_2 hydrate density
C_{ph}	2220J/kg•K	Hydrate heat capacity
C_{pn}	860 J/kg•K	Specific heat capacity of CO_2
C_{pw}	4200 J/kg•K	Specific heat capacity of water
C_{ps}	920 J/kg•K	Heat capacity of silty sand formation
ρ_s	2650 kg/m^3	Sand silt formation density
k_w	0.50W/m•K	The thermal conductivity of water
k_c	0.060W/m•K	Thermal conductivity of liquid CO_2
k_s	2.31W/m•K	Thermal conductivity of sand silt
k_h	0.39W/m•K	Thermal conductivity of hydrate

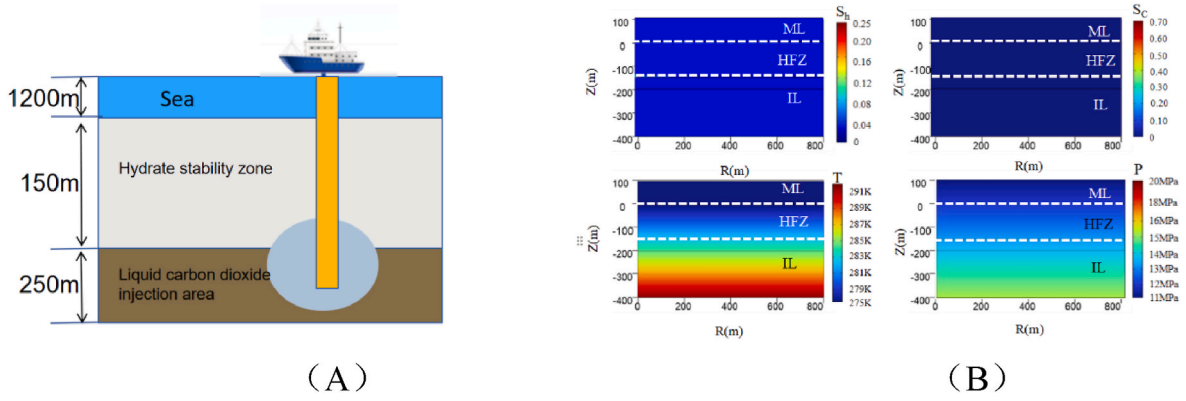

Fig. 1. (A) Marine sandy silty carbon dioxide injection well storage diagram (B) Initial distribution of hydrate saturation, CO_2 saturation, pressure, and temperature in the reservoir.

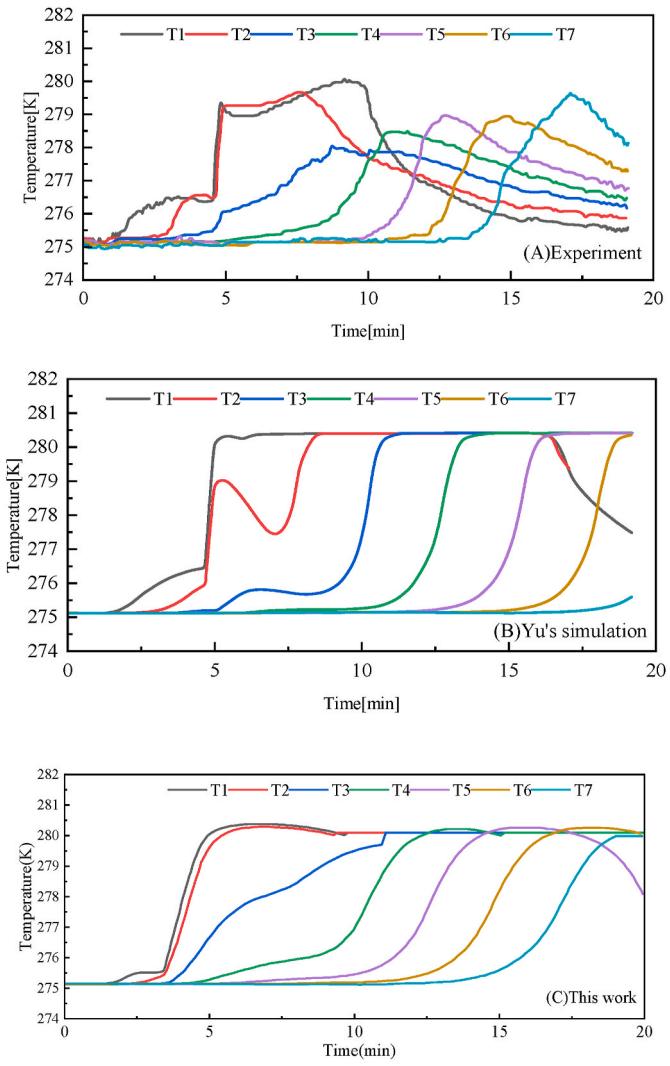

Fig. 2. Comparison of simulation results of this model with experimental data and other simulation work. (A) Experimental results of temperature changes detected at T1-T7 (Inui et al., 2011); (B) Simulation results by Yu et al. (Yu et al., 2016); (C) Simulation results of this exercise.

formation of hydrate cap is critical for understanding the behavior of key parameters in CO_2 storage simulations. This understanding helps to clarify the internal mechanisms of CO_2 hydrate sequestration and the formation of a closed system in sandy silty strata. For this analysis, the conditions considered include a CO_2 injection pressure of 16 MPa, an injection temperature of 8 °C, permeability of 100mD, water saturation of 0.8, and porosity of 0.3. These parameters were applied to marine sediment strata for detailed investigation. The injection well is positioned 200m below seafloor, corresponding to a depth of $d_{mbsf} = 200$m, with coordinates (0,-200m).

Fig. 3 reveals the dynamic evolution process of CO_2 saturation and temperature and pressure before forming the hydrate cover. By the 200th day of injection, CO_2 saturation near the injection well begins to change, reaching approximately 0.3. CO_2 diffuses in a semi-elliptical pattern with a radius of about 20m. During this period, the formation temperature decreases from 283K to 281K, while the formation pressure rises significantly from 14 MPa to 16 MPa. Temperature changes are not as obvious as pressure changes. Experiments also indicate that the heat transfer during CO_2 hydrate formation in porous media is limited (Hosseini Zadeh et al., 2023). From day 200 to day 600 of injection, the trends become more pronounced, indicating that CO_2 continues to spread within the sandy silty strata. At this stage, the CO_2 saturation at the injection point reaches its peak value of 0.7, diffusing outward from the injection point, with the formation temperature following a similar decreasing trend. The formation pressure near the injection well remains around 16 MPa, with slight increases in the surrounding formation pressure. The pressure increase is more pronounced below the injection depth than above.

Fig. 4 illustrates the changes in hydrate and CO_2 saturation, along with variations in formation temperature and pressure during the formation of the hydrate cap. After the formation of the hydrate cap layer (By day 1953), the edge of the liquid CO_2 saturation zone reaches 50mbsf, and the hydrate cap layer prevents the further upward flow of CO_2. The 281K isotherm around the injection well expands slightly, although most of the formation remains in its initial thermal state due to the high thermal conductivity(3.1W/m·K) of the sandy silt. Finally, due to the heat exchange with the surrounding environment, the final formation temperature tends to the initial injection well temperature (during in the days 4000–5000). This result is validated by recent simulation work using the Tough + Hydrate software (Gu et al., 2025). As the cap layer grows (2000–5000 days), the high saturation range of liquid CO_2 in the center of the injection storage area expands significantly, and the marginal range of CO_2 saturation spreads laterally in the 100–200 mbsf region. The hydrate cover extends laterally to 150 m and longitudinally to 20 mbsf, showing a trapezoidal shape with a wide upper boundary and a narrow lower boundary. The area and volume of CO_2 hydrate are key factors in determining the effectiveness of CO_2 sealing and assessing the risk of CO_2 leakage (Guo et al., 2024). At the completion stage (By day 5000), the hydrate cap extends laterally to 400 m and longitudinally to −150 mbsf. The highly saturated region of liquid CO_2 diffuses horizontally to 200–400 m.

3.2. *Efficient CO_2 formation parameters*

This section analyzes the effects of formation conditions such as initial permeability, porosity, and water saturation on CO_2 sequestration, and provides a reference for selecting suitable reservoir conditions. The injection well parameters remain constant, with the well located at 175m below the seafloor ($d_{mbsf} = 175$m), corresponding to coordinates (0,-175m). To comprehensively assess parameter influences on well injection under representative conditions, randomized screening within the experimental ranges (8–11 °C, 14–20 MPa) was conducted to select typical working conditions: 20MPa/8 °C for permeability analysis, 14MPa/10 °C for porosity studies, and 18MPa/10 °C for water saturation investigations. This randomized selection approach ensures the simulation conditions effectively capture the overall system behavior while maintaining experimental validity. The chosen parameters (temperature varying between 8 and 10 °C and pressure ranging from 14 to 20 MPa) were strategically distributed across the operational envelope to provide a representative characterization of the injection process.

3.2.1. *Impact of initial permeability*

Fig. 5 presents the simulated results for CO_2 injection at a pressure of 20 MPa and a temperature of 8 °C, with permeability of 100mD, 200mD, 300mD, and 400mD respectively. The figure illustrates changes in CO_2 storage rate and gas storage capacity in the sandy silty formation. As permeability increases, the time required for hydrate formation and sequestration decreases. Specifically, when the permeability is 100 mD, sealing capacity reaches its maximum, which is the most favorable condition for CO_2 storage.

3.2.2. *Influence of initial porosity*

As shown in Fig. 6, changes in CO_2 sequestration rate and gas storage capacity in the sandy silty formation are analyzed for initial porosities of 0.3, 0.35, and 0.4 under a CO_2 injection pressure of 14 MPa and a temperature of 10 °C. The figure shows a slight decrease in sealed stock with increasing porosity. When the porosity is 0.3, the maximum net CO_2 storage is achieved. Although higher porosity theoretically allows

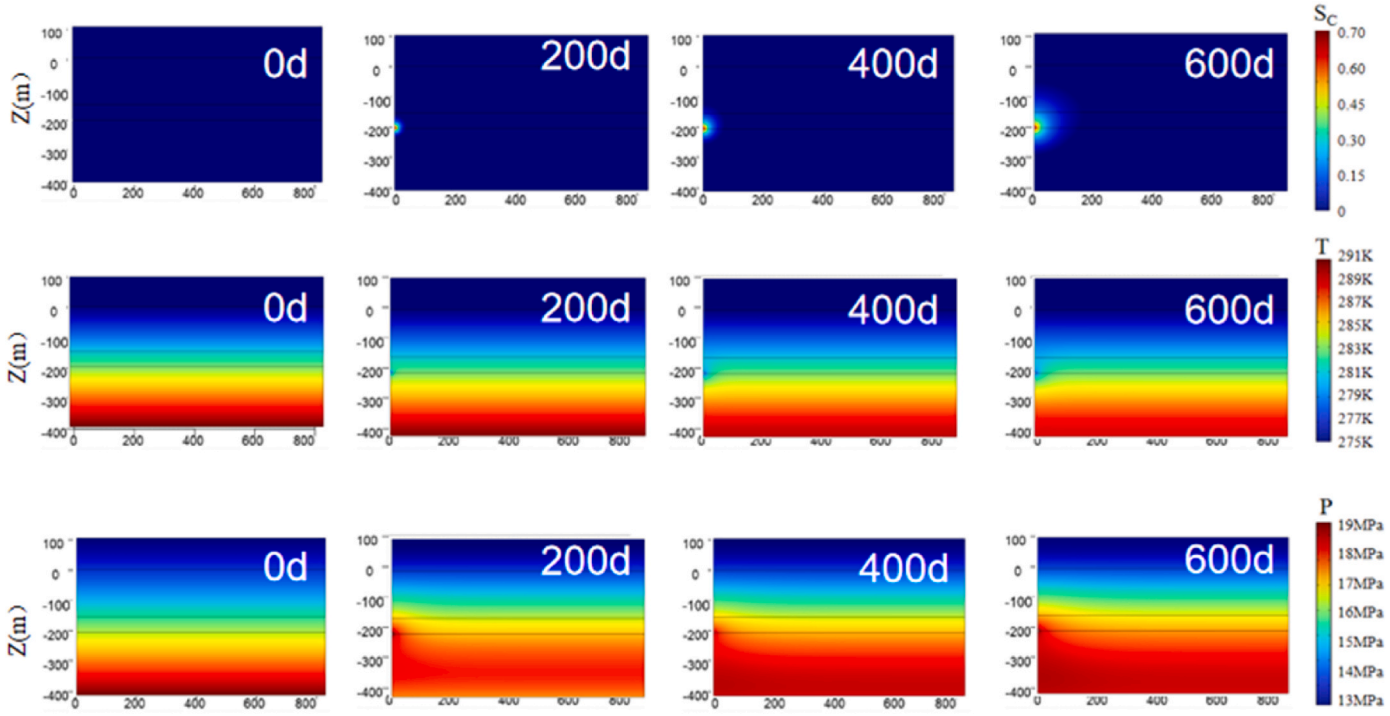

Fig. 3. Changes of CO_2 saturation, temperature, and pressure before the formation of the hydrate cap layer in the sandy silty formation.

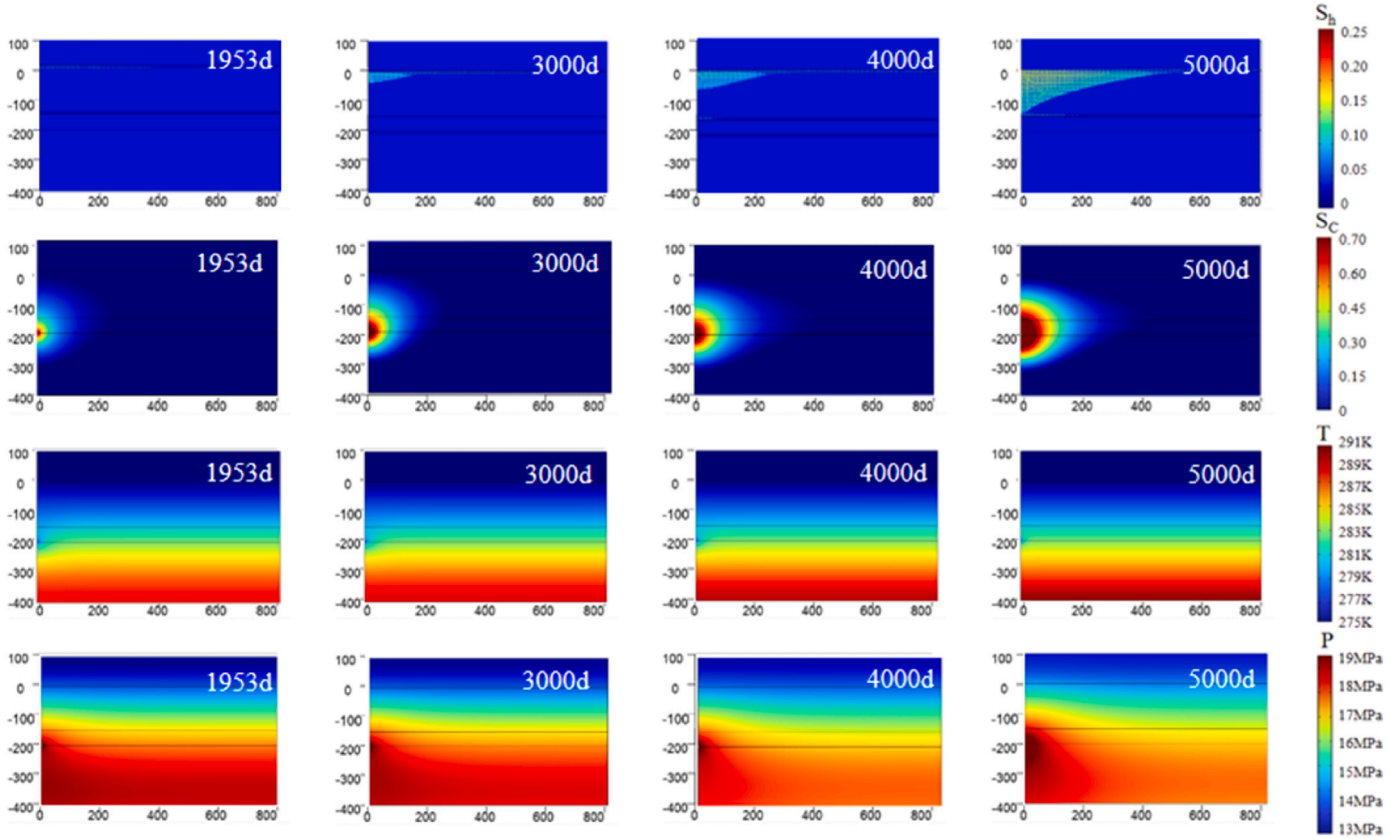

Fig. 4. Changes in hydrate saturation, CO_2 saturation, temperature, and pressure during the formation of hydrate cap layer in the sandy silty formation.

for greater gas storage, leading to increased sealed stock, the saturation of the sealed gas does not reach its maximum. Excess water and air remain in the pore space, so the actual results indicate that the initial porosity has a minor effect on the final sealed stock and a greater impact on the permeability. In addition, it is important to note that the model only modified the formation porosity, without altering the absolute

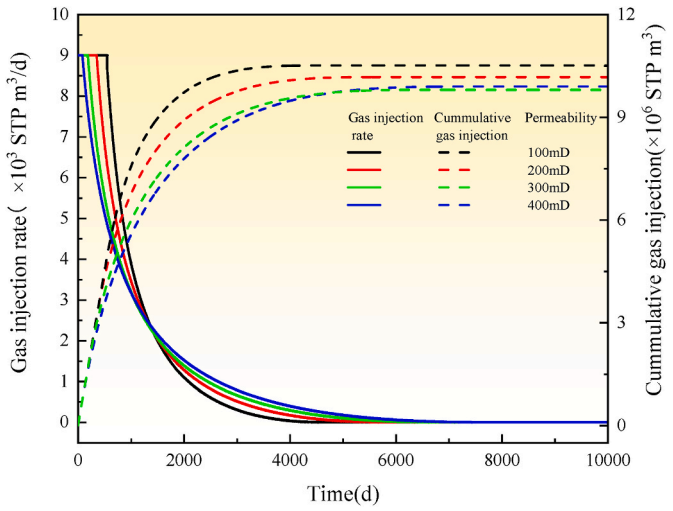

Fig. 5. Effects of sandy silty formation and different initial permeability on sealing rate and sealing quantity (injection pressure 20 MPa, temperature 8 °C).

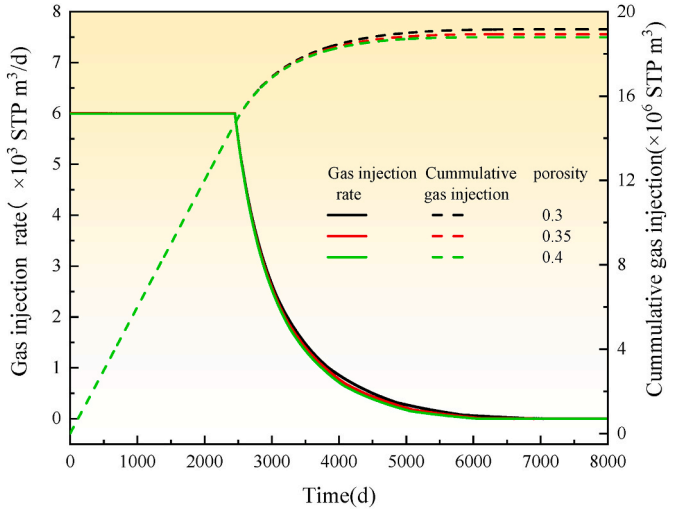

Fig. 6. Effects of sandy silty formation and different initial formation porosity on sealing rate and storage volume (injection pressure 14 MPa, temperature 10 °C).

permeability of the cap layer. In practical scenarios, absolute permeability and porosity are positively correlated, meaning that higher porosity often corresponds to higher absolute permeability.

3.2.3. *Influence of initial water saturation*

As shown in Fig. 7, the effects of initial water saturation on CO_2 storage rate and gas storage capacity in the sandy silt-sand formation were analyzed under an injection pressure of 18 MPa and an injection temperature of 10 °C, with water saturations of 0.3, 0.6, 0.8, and 0.9, respectively. When the water saturation is less than 1, the initial formation contains gases other than pore water that do not participate in the reaction, and its composition can be dominated by air, such as nitrogen. At the same temperature and pressure, hydrate nucleation occurs at 1453 days. The final sealed stock decreases with increasing initial water saturation. Liu et al. (2024b) found that in the residual area of seawater (where water saturation is relatively low), hydrate predominantly forms in sheet-like structures, forming granular cement, whereas in the saturated seawater zone, hydrate forms from the center of the pores and is distributed in a granular manner. Poor pore connectivity and limited gas-liquid contact in the saturated zone hinder further

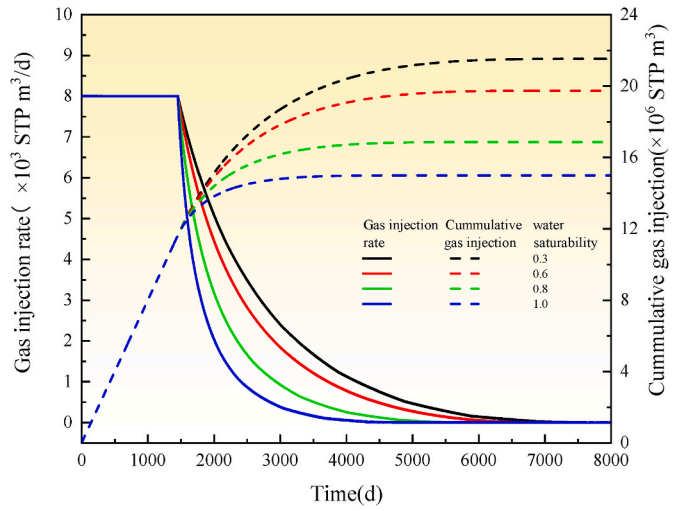

Fig. 7. Effect of initial water saturation on storage rate and storage capacity (CO_2 injection pressure 18 MPa, temperature 10 °C).

hydrate formation, resulting in a final hydrate saturation that is at least 25 % lower than that in the residual area of seawater. Aghajanloo et al. 's experiment also showed that the saturation of CO_2 hydrate increased with water saturation, and the hydrate would clog the pore faster (Aghajanloo et al., 2024). These studies explain why CO_2 storage capacity is the largest when water saturation is low. In conclusion, formations with low water saturation are optimal for CO_2 storage in sandy silty strata.

3.3. *Efficient CO_2 injection well parameters*

The initial phase of CO_2 sequestration in a reservoir typically involves assessing the geological structure, including factors such as volume, injection rate, capping mechanisms, and capacity characteristics. These assessments are crucial for determining the feasibility of reservoir CO_2 sequestration (Aminnaji et al., 2024). In this section, a formation with an initial permeability of 100 mD, porosity of 0.3, and water saturation of 0.8 is selected to examine the effect of efficient injection temperature and pressure parameters on sealing rate and capacity. It is worth noting that the reason for selecting the hydrate saturation of 0.8 for the study is that although it was found in previous studies that low saturation can store more CO_2, the water saturation of sandy strata suitable for sequestration in the potential reservoir sandstone in the South China Sea at a depth of 1200 m is around 0.8.

3.3.1. *Injection well temperature*

As shown in Fig. 8(A), the injection well is located 175m below the seafloor (d_{mbsf} = 175m), with an injection pressure of 20 MPa. The impact of injection well temperature on gas storage rate and capacity during CO_2 storage in sandy silt-sand formation is analyzed. The trapped stock initially increases at a constant rate before hydrate formation, but slows down and eventually reaches 0 after hydrate formation.

At a CO_2 injection pressure of 20 MPa, Fig. 8(B) illustrates the changes in hydrate and CO_2 saturation under different injection temperatures after forming the closed hydrate layer. Following the formation of the closed layer, the hydrate cover layer presents an approximately arc-shaped distribution. At 8 °C, the hydrate diffuses laterally to 450m and longitudinally to −150m, with maximum hydrate saturation reaching approximately 0.15. The hydrate saturation at the edge of the cap layer is around 0.1. As the increase of injection temperature, the hydrate saturation within the cap layer increases gradually, with maximum hydrate saturation reaching 0.2–0.25 at 11 °C. The CO_2 saturation distribution forms an elliptical pattern. At 8 °C, CO_2 spreads 250 m horizontally and 50–300 mbsf longitudinally. The CO_2

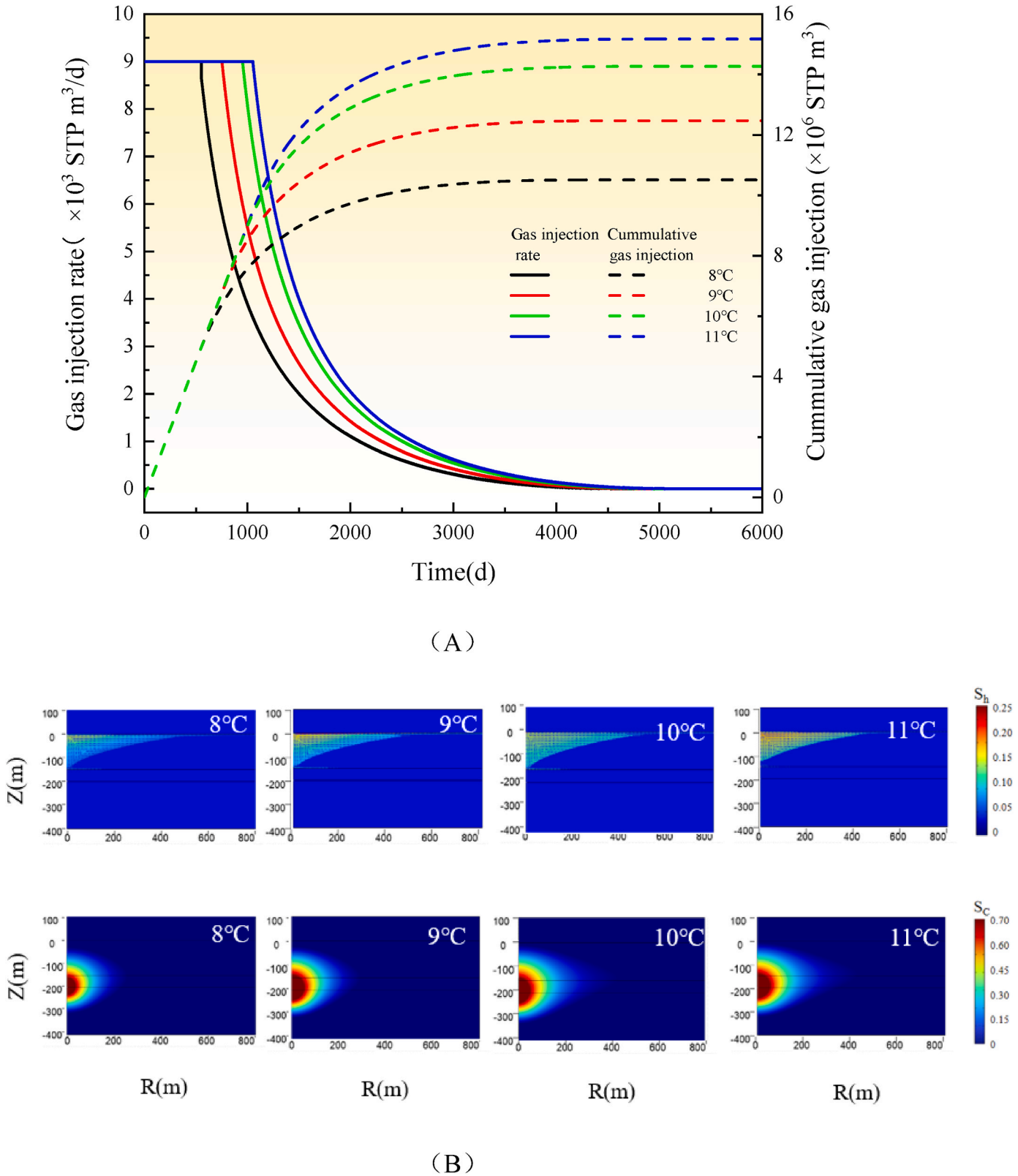

Fig. 8. CO_2 injection pressure is 20 MPa and d_{mbfz} = 175m: (A) Relationship between storage rate and storage capacity at different injection temperatures (B) Relationship between hydrate saturation and carbon dioxide saturation distribution at different injection temperatures after the formation of the closed layer.

saturation is highest at the center, around 0.7, and gradually decreases outward until it reaches 0. At 9 °C, CO_2 diffuses horizontally to 300 m, with a longitudinal diffusion range of 20~300mbsf longitudinally. At 10 °C and 11 °C, CO_2 diffuses 400 m horizontally and between −0 and 300mbsf longitudinally. The cloud diagram indicates that the CO_2 approaches the seabed, with some CO_2 leaking into the seawater layer. Due to the constraints imposed by the cap layer, CO_2 at 10 °C and 11 °C exhibits lateral seepage. The light blue region of CO_2 saturation is

observed between 100 and 200mbsf, and the lateral diffusion increases to nearly 400m.

In general, the diffusion range of CO_2 expands with the increase of temperature, but the increase of CO_2 saturation is not obvious at 10 °C and 11 °C. This is due to excessive CO_2 leakage on the one hand, and when the initial injection temperature approaches or begins to exceed the phase equilibrium temperature, the amount of hydrate formation will decrease (Zhang et al., 2024). CO_2 saturation reaches its peak at 11 °C.

As shown in Fig. 9, the injection well is located 175m below sea level (d_{mbsf} = 175m), with a CO_2 injection pressure of 20 MPa. The effect of injection temperature (8 °C, 9 °C, 10 °C and 11 °C) on the leakage rate and amount during CO_2 storage in the sandy silt-sand formation is analyzed. As the temperature increases, the time to the onset of leakage shortens. At 8, 9, 10, and 11 °C under 20 MPa pressure, carbon dioxide diffuses beyond the hydrate formation zone, with leakage into the ocean occurring after 403, 323, 253, and 192 days. After maintaining a steady rate for some time, the leakage experiences a period of fluctuation and gradual decline as the hydrate cap layer forms. By around 4000–5000 days, as the cap layer becomes fully established, the leakage approaches 0. The simulation indicates that the hydrate cover effectively mitigates CO_2 leakage. The simulation results of Sawano et al. (2022) show that when the formation permeability exceeds 10^{-12} m^2 (1 mD), leakage phenomenon occurs and leaked CO_2 can reach the seafloor. In this paper, the permeability of sandy silt is 100-400mD, and leakage phenomenon also occurs. However, Sawano et al. (2022) believe that the formation of CO_2 hydrate cannot inhibit the leakage of liquid CO_2, and the simulation in this paper show that the complete formation of hydrate cap can effectively prevent the leakage of CO_2. This was also verified experimentally: Zhao et al. (2023) used MRI visualization system to observe that the formation of the cap layer of CO_2 hydrate can effectively prevent the leakage of dioxide. Overall, CO_2 leakage increases with rising injection temperature and the hydrate seal can effectively reduce the leakage of CO_2.

3.3.2. *Injection well pressure*

As shown in Fig. 10(A), when the injection well is located 175m below seafloor (d_{mbsf} = 175m) and the CO_2 injection temperature is 8 °C, the impact of injection well pressure on the sequestration rate and gas storage during CO_2 sequestration in the sandy silt-sand formation is analyzed. Before the formation of the hydrate cap layer, the sealed stock increases at a constant rate, but this growth slows down and approaches zero after the cap layer forms. The sealed stock decreases as injection pressure increases. The reason is that although higher initial pressure is high allows for faster CO_2 injection, excessive pressure can lead to significant CO_2 seepage and leakage into the ocean. Additionally, rapid hydrate cap formation hinders further CO_2 injection. In conclusion, for sandy silty formations with high permeability, moderate CO_2 injection under lower injection pressure is more suitable.

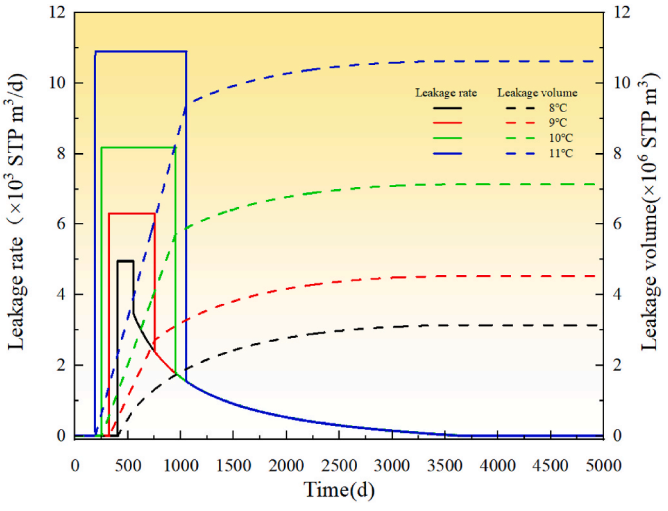

Fig. 9. The relationship between the leakage rate, leakage amount, and different injection temperatures at a CO_2 injection pressure of 20 MPa and d_{mbfz} = 175m.

Under a CO_2 injection well temperature of 8 °C and different injection pressures, changes in hydrate and CO_2 saturation after the formation of the closed layer are depicted in Fig. 10(B). Following the formation of the closed layer, the hydrate cover layer forms a curved structure. At 14 MPa, lateral hydrate diffusion reaches 450 m, and the longitudinal diffusion reaches 150 mbsf. The saturation of the hydrate reaches the maximum in the 0–10 mbsf range at around 0.2, while saturation at the edge of the cap layer is approximately 0.15. As injection pressure increases, hydrate saturation in the cap layer rises, with a maximum value of 0.25 at 20 MPa. The CO_2 saturation distribution forms an oval pattern. At 14 MPa, CO_2 spreads 250 m laterally and 50–300 mbsf longitudinally, with a center saturation of approximately 0.7, gradually decreases outward until it drops to 0. At 16 MPa, lateral CO_2 diffusion reaches 400m, with longitudinal diffusion from 0–300 mbsf. At 10 °C and 11 °C, the transverse diffusion of CO_2 reaches 400m, with a longitudinal diffusion range of 0-300mbsf. The cloud image shows that CO_2 diffusion extends close to the seabed, with some CO_2 leaking into the seawater layer. Due to the restriction of the cap layer, at injection pressures of 18 MPa and 20 MPa, CO_2 exhibits a lateral seepage trend. The light blue CO_2 saturation area is located between 100 and 200 mbsf area, and the transverse area expands to nearly 400m. Overall, with the increase of pressure, the diffusion range of CO_2 gradually expands, and the center area of CO_2 high saturation increases accordingly.

As shown in Fig. 11, the injection well is located 175 m below seafloor (d_{mbsf} = 175m), with a CO_2 injection temperature of 8 °C and injection pressures of 14,16,18 and 20 MPa. The effect of these pressures on the leakage rate and amount during CO_2 storage in the sandy silt-sand formation is analyzed. As injection pressure increases, the time to the onset of leakage decreases. At 8 °C, 14, 16, 18, and 20 MPa, CO_2 diffusion exceeds the hydrate formation zone, and the corresponding times of leakage into the ocean are 1153, 853, 553, and 403 days, respectively. For approximately 150 days, leakage occurs at a constant rate, after which, with the formation of the hydrate cap layer, the leakage experiences fluctuations followed by a slow decline. Since the rate of flow of CO_2 in the water and sedimentary layers is basically close to the formation initial temperature pressure. The generation of hydrate is dominated the characteristic kinetics. So the leakage rate is very close, and the rate curve is close to consistent. By 4000–5000 days, as the cap layer becomes fully formed, the leakage approaches zero.

Fig. 12 presents the three-dimensional column charts of (A) sealed quantity and (B) leakage quantity under different injection temperatures and pressure with the well located 175m below sea level (d_{mbfz} = 175m). At the same pressure, both the sealed and leakage quantities increase as the temperature rises (Fig. 12(A)). At the same temperature, the storage volume generally decreases with increasing pressure, except at 11 °C, where the sealing capacity increases slightly from 19.19 to 19.28 × 10^6 $STPm^3$. Chen et al. (2024)experimentally demonstrated that the CO_2 storage in the form of hydrate in the muddy silt systems was 60 % higher than in the sandy systems. This numerical simulation confirms that conclusion, showing that the maximum storage capacity of muddy silt at the site scale could reach 25.84 × 10^6 $STPm^3$, exceeding that of sandy silt. Leakage quantity increases with rising pressure, and the leakage amount increases significantly at 18–20 MPa, as shown in Fig. 12(B). Overall, the total leakage and storage quantities increase with rising temperature and pressure, aligning with physical expectations. By selecting conditions that optimize both a higher sealed quantity and a lower leakage quantity, the most suitable conditions for CO_2 storage in sandy silty formations are at a temperature of 10 °C and a pressure of 14 MPa. Under these conditions, the sealing quantity is 19.19 × 10^6 $STPm^3$ and the leakage amount is 1.84 × 10^6 $STPm^3$.

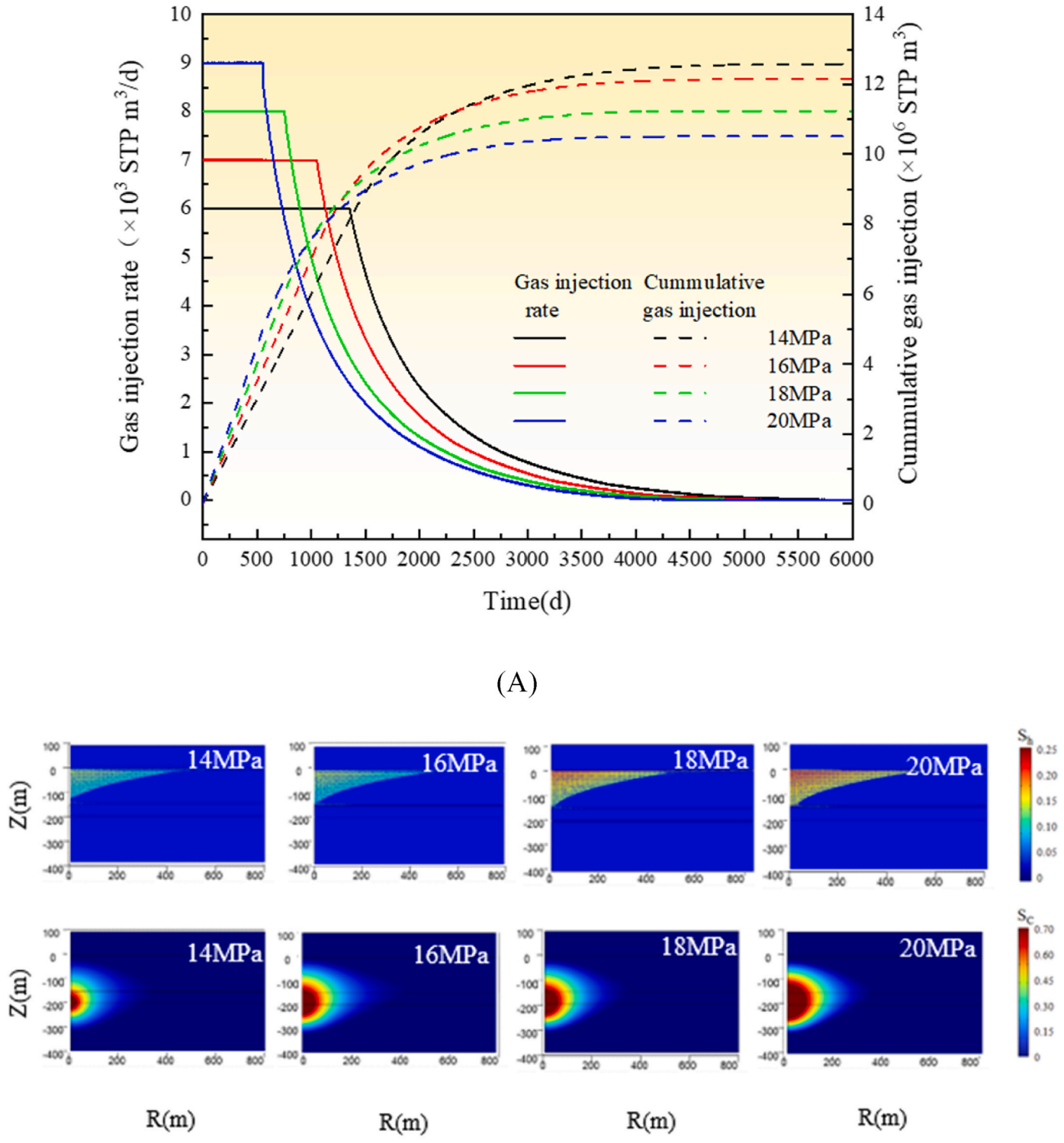

Fig. 10. CO_2 injection temperature of 8 °C and d_{mbfz} = 175m (A) Relationship between storage rate and storage capacity at different injection pressures (B) Relationship between hydrate saturation and carbon dioxide saturation distribution at different injection pressures after the formation of the closed layer.

3.3.3. *Injection well location*

According to previous studies, selecting moderate temperature and pressure conditions is suitable for CO_2 injection in sandy silt formations. As the formation pressure increases from 13.75 MPa (d_{mbfz} = 175m) to 15.5 MPa (d_{mbfz} = 350m) with the rise of the formation, the unified injection well condition of 14 MPa cannot be maintained due to excessive formation pressure. Therefore, in this section, the CO_2 injection temperature of 8 °C and the injection pressure of 16 MPa were selected to investigate the effects of different vertical well locations on the gas storage rate and capacity during CO_2 storage in the sandy silt-sand

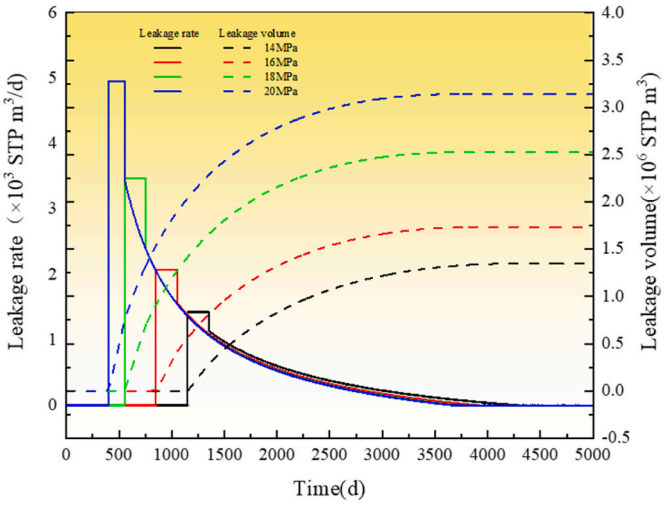

Fig. 11. Relationship between the leakage rate, leakage amount, and different injection pressures at a CO_2 temperature of 8 °C and d_{mbfz} = 175m.

formation, as illustrated in Fig. 13. The injection rate is first injected at a constant rate of 7 × 10^3STPm^3/d. As the injection position moves further from seafloor, corresponding to hydrate formation at depths of 175 m, 200 m, 250 m, and 350 m hydrates, the sequestration time increases to 1,052, 1203, 1513, and 1813 days, respectively. Once the hydrate cap layer forms, the injection rate declines to 0 between 5000 and 6000 days, marking the completion of the sealing process.

Fig. 14 shows the simulation results of the effects of a CO_2 injection temperature of 8 °C, pressure of 16 MPa, and vertical well location at 175 m, 200 m, 250 m, and 350 m below seafloor on the leakage rate and leakage amount during CO_2 storage in sandy silty formation. As the distance from the seafloor to the injection location increases, the CO_2 leakage time increases gradually. At 16 MPa at 8 °C, the CO_2 leakage times corresponding to well depths of 175 m, 200 m, 250 m, and 350 m below seafloor are 1153, 1303, 1613 and 1313 days, respectively, which occur slightly after the formation of the hydrate cap layer. The rate of decline is relatively close, mainly because the location of the leak is far from the injection well, and the temperature and pressure conditions are similar to the initial silty sand formation. The leakage quantity decreases as the distance from the injection well increases.

As shown in Fig. 15, increasing the injection depth results in a corresponding increase in the sealed stock and a decrease in the leakage volume. The increase in sealed stock is attributed to the longer time required for the sequestration rate to decline with greater injection depth (As shown in Fig. 13). The decrease in leakage is due to the longer time it takes for CO_2 to migrate to the seafloor as injection depth increases, thus extending the leakage time (As shown in Fig. 14). Increasing the injection well depth appropriately facilitates higher CO_2 storage in the sandy silty formations with higher permeability, while also reducing CO_2 leakage.

Under an injection well temperature of 8 °C and pressure of 16 MPa, the distribution cloud maps of CO_2 hydrate saturation (a-d) and CO_2 saturation (e-h) after the formation of the hydrate cap layer are shown in Fig. 16. In Fig. 16(a–d), the shape of the cap layer is approximately curved. When the injection well is located 175 m below seafloor (d_{mbsf} = 175m), the lateral radius of the hydrate cap layer is 200 m and the longitudinal diameter is 40mbsf (As shown in Fig. 16(a)). When d_{mbsf} = 200m, the lateral radius and longitudinal diameter of the hydrate cover layer expand to 450 m and 150 mbsf (As shown in Fig. 16(b)), and the hydrate saturation is higher compared to the d_{mbsf} = 175m. Hydrate saturation reaches its maximum within the range of −10m~0m. At d_{mbsf} = 250m, the lateral radius increases to 550m, and the longitudinal diameter is 120 mbsf, though hydrate saturation decreases (As shown in Fig. 16(c)). When d_{mbsf} = 350m, the lateral radius of the hydrate cover is approximately 500 m, and the longitudinal diameter is 100 mbsf (As shown in Fig. 16(d)), with a further decrease in hydrate saturation compared to d_{mbsf} = 250m. The analysis shows that as the depth of the injection well increases, the formation range of the hydrate cap initially increases and then decreases, while hydrate saturation follows a similar trend, peaking when the injection well location is d_{mbsf} = 200 m.

When d_{mbsf} = 175m, the fluid CO_2 percolation shape is approximately elliptical, with a transverse percolation of 220 m and a longitudinal percolation of 50-300mbsf, where most of the CO_2 percolation occurs in the range of 50~220 mbsf (as shown in Fig. 16(e)). When d_{mbsf} = 200m, the fluid CO_2 percolation shape becomes roughly rugby ball shape, with a transverse CO_2 percolation of 400m, and a longitudinal CO_2 percolation of 0-320mbsf. The percolation distance increases within the range of 120–250 mbsf due to the influence of the cap layer (as

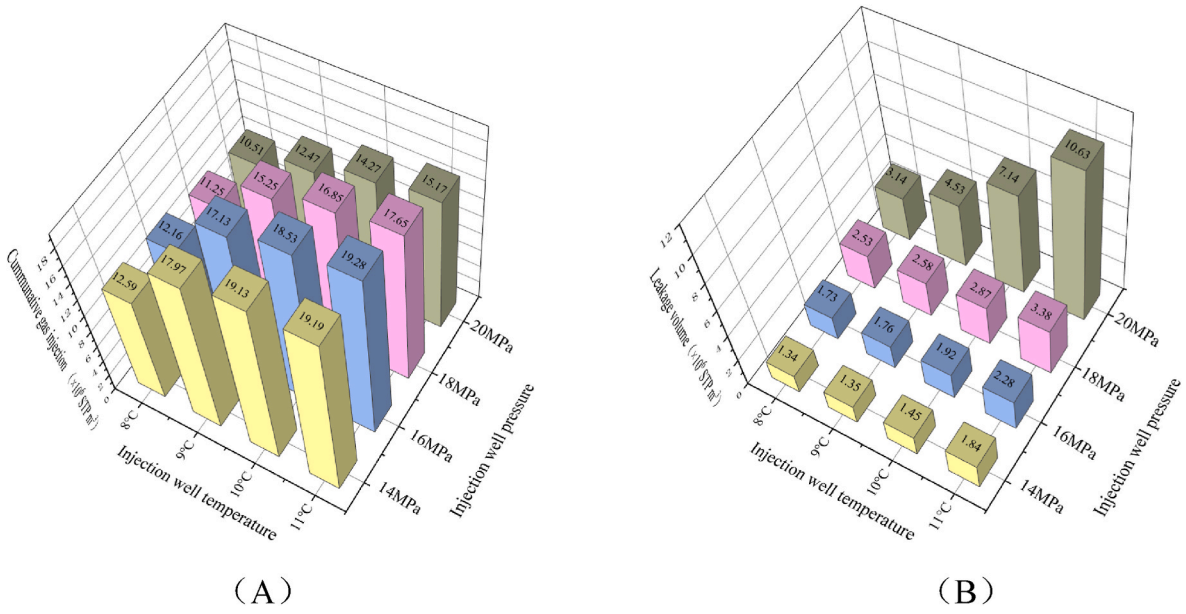

Fig. 12. Three-dimensional histogram of (A) containment volume and (B) leakage volume at different injection temperatures and pressures with the injection well located 175 m below sea level.

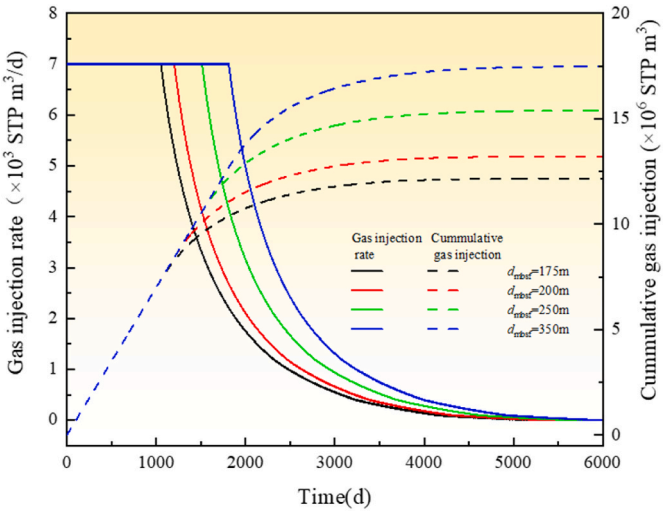

Fig. 13. Relationship between the sequestration rate and gas storage at different injection locations with CO_2 temperature of 8 °C and a pressure of 16 MPa.

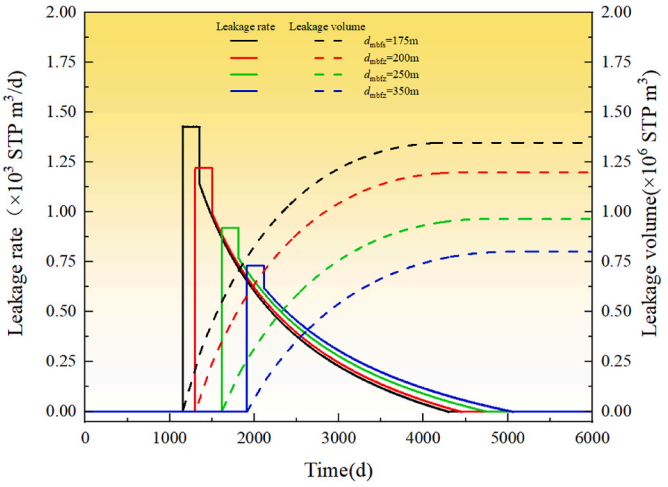

Fig. 14. Relationship between the leakage rate and leakage volume at different injection positions with CO_2temperature of 8 °C and the pressure of 16 MPa.

shown in Fig. 16(f)). At $d_{mbsf} = 250$m, the center of gravity of the rugby ball-shaped CO_2 percolation drops, with transverse percolation reaching 400m and longitudinal percolation extending from 0 to 120mbsf. The diffusion is significant at the edge, within the 200m–280 mbsf range (as shown in Fig. 16(g)). When $d_{mbsf} = 350$ m, the flow shape of liquid CO_2 resembles a mushroom cloud, with a transverse flow of CO_2 of 400m, and a longitudinal flow ranging from 50 to 400mbsf. In the low saturation range of 300~400 mbsf, the cap layer enhances transverse flow, leading to the highest CO_2 saturation (as shown in Fig. 16(h)).

The cloud image analysis reveals that the location of the injection well and the hydrate cap layer together affect the final distance and morphology of CO_2 seepage. As the injection well depth increases, a larger lateral diameter hydrate cap layer and a broader CO_2 seepage range are formed. This explains the result shown in Fig. 15, where increasing injection depth leads to higher sealed stock and reduced leakage. In other words, the larger cap zone and expanded CO_2 range contribute to increased sealed stock and reduce leakage. This further supports the conclusion that CO_2 sequestration in sandy silty formations is enhanced as the injection depth increases in the range of 150–400 mbsf.

The comparative analysis in Fig. 17 demonstrates distinct trends in

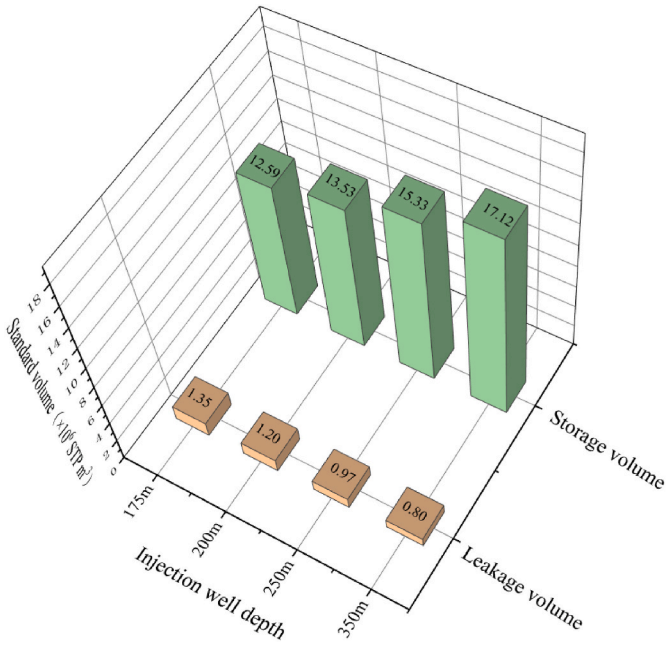

Fig. 15. Comparison of sealed stock and leakage at different injection well locations in sandy silty formation.

CO_2 phase distribution across the six-stage sealing period (each stage lasting 1000 days), revealing that the stockpile growth rate during 0–2000 days was approximately 3.5 times faster than during 2000–6000 days. As shown in Fig. 17, the proportion of CO_2 stored in hydrate form increased progressively from less than 3 % in initial stages to about 30 % when storage completion was achieved at 5000–6000 days. The figure further illustrates depth-dependent variations in hydrate phase storage efficiency (hydrate-bound CO_2 to total stored CO_2 ratio), with values of 25 % at 175mbsf (corresponding to the smallest storage area of 3.04×10^6 STP m^3 in Figs. 16a), 33 % at 200mbsf, 37 % at 250mbsf, and 31 % at 350mbsf (representing the largest storage area of 5.41×10^6 STP m^3 in Fig. 16d, where printability was highest). Throughout the process documented in Fig. 17, the dissolved phase maintained a stable about 29 % proportion of CO_2 capture (Xia et al., 2025), while the liquid CO_2 phase dominated initial storage (40–70 %) before decreasing as hydrate formation increased in later stages. These findings highlight the complementary storage mechanisms, with liquid CO_2 being crucial for early injection, dissolved phase providing stable retention, and hydrate formation becoming increasingly significant for long-term sequestration, particularly at optimal depths around 350mbsf where both storage capacity and efficiency peak.

4. Conclusion

This article investigates whether there will be any leakage during the storage of CO_2 in suitable marine formations in the South China Sea, the extent of any potential leakage, and whether it can be mitigated or even completely avoided by forming hydrate cover layers to address the aforementioned issues.

Research shows the final sealed stock decreases with increasing initial formation permeability and the sealed stock also decreases as initial water saturation increases. Formation porosity has little effect on storage capacity. At the same injection pressure, sealed stock and leakage will increase with the increase in injection temperature. At the same injection temperature, increasing injection pressure results in a decrease in sealed stock and an increase in leakage. As injection depth increases, the time for the sequestration rate to decline increases, leading to an increase in sealed stock, a longer time for CO_2 to percolate to sea level, and a corresponding reduction in leakage. The final shape of

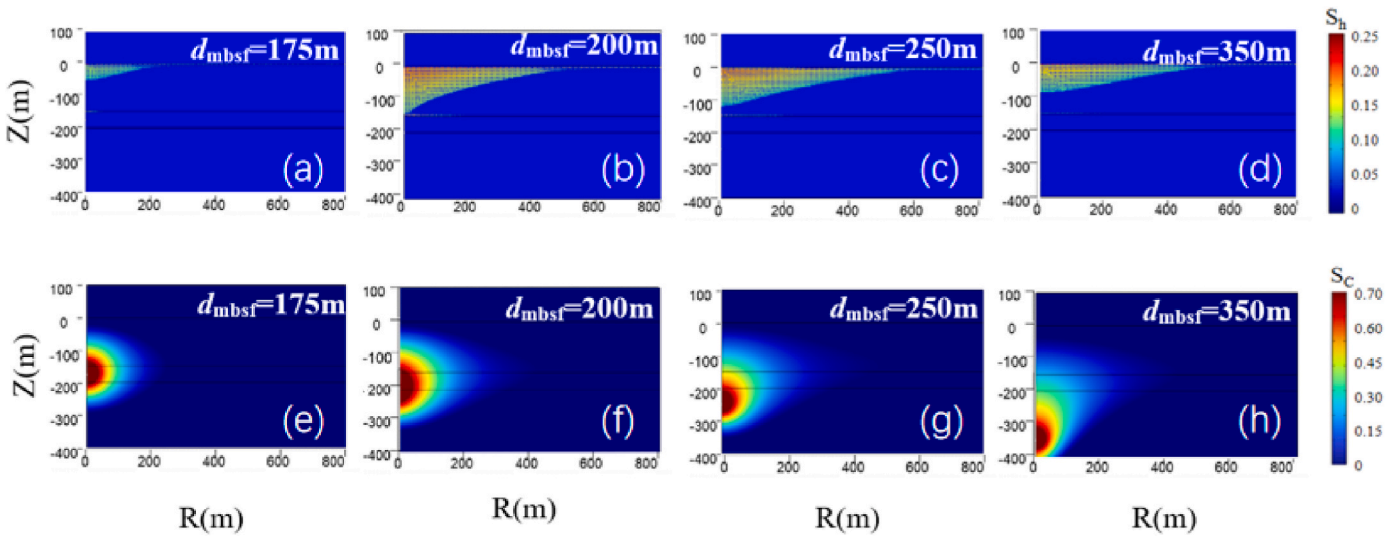

Fig. 16. CO_2 hydrate saturation (a–d) and liquid CO_2 saturation distribution (e–h) at different injection locations in sandy silt after hydrate cap formation. (CO_2 injection temperature 8 °C, pressure 16 MPa).

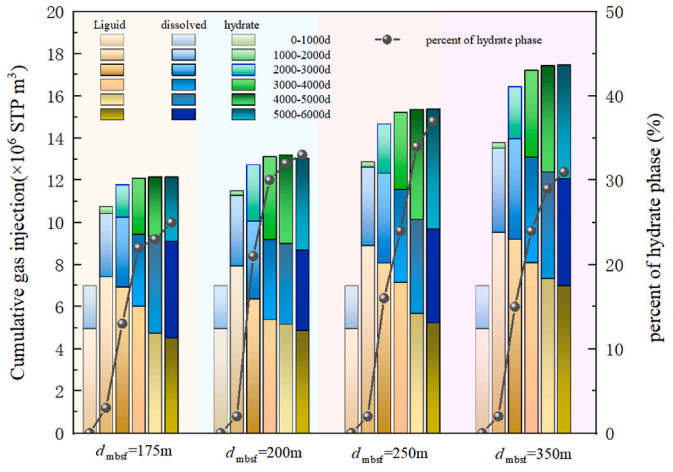

Fig. 17. The relationship between the amount and proportion of each phase of liquid, dissolved and hydrate injected into the reservoir to the basic completion (0–6000days) of the storage for every thousand days under different well injection locations.

the marine sandy silt hydrate cap is a cone. The temperature increase in the formation remains minimal, with the final temperature range consistent with that of the injection well extending from the wellhead. The location of the injection well and the hydrate cover affect the final distance and morphology of CO_2 seepage. With the increase of injection well location, a larger lateral diameter hydrate cap layer and liquid CO_2 seepage range can be formed.

This research result is important because it tells researchers on ocean carbon sequestration that controlling CO_2 injection pressure and injection position can effectively regulate the formation process of hydrate cap layers, while the influence of injection temperature is relatively small.

In the future, based on the model proposed in this work, the formation process of CO_2 hydrate carbon sequestration cover layers in different depths of marine formations and muddy silt formations can be studied to determine the sequestration effect and leakage situation. The hydrate formation equation could be adapted to satisfy CO_2 sequestration scenarios in extreme conditions as supercritical CO_2.

CRediT authorship contribution statement

Mengyang Li: Writing – original draft, Investigation, Formal analysis, Data curation. **Shuanshi Fan:** Writing – review & editing, Supervision, Conceptualization. **Yanhong Wang:** Project administration, Formal analysis, Data curation. **Xuemei Lang:** Validation, Resources. **Gang Li:** Writing – original draft, Validation, Methodology, Formal analysis.

Declaration of competing interest

The authors declare that they have no known competing financial interests or personal relationships that could have appeared to influence the work reported in this paper.

Acknowledgments

This work was supported by the Special Project for Marine Economy Development of Guangdong (six marine industries) (GDNRC[2024]33), Key Research & Development Program of Guangzhou (No.202206050002), and National Natural Science Foundation of China (21736005 and 51876069).

Data availability

Data will be made available on request.

References

Aghajanloo, M., Taghinejad, S.M., Voskov, D., Farajzadeh, R., 2024. Influence of water saturation and water memory on CO2 hydrate formation/dissociation in porous media under flowing condition. Chem. Eng. J. 492, 152455.

Agrawal, R., Kumar, Y., Sarkhel, R., Damdhar, M.S., Sangwai, J.S., 2023. Enhancing the CO2 sequestration potential in subsea terrain by hydrate formation from liquid CO2. Energy Fuels 37, 14961–14976.

Ajayi, T., Gomes, J.S., Bera, A., 2019. A review of CO2 storage in geological formations emphasizing modeling, monitoring and capacity estimation approaches. Pet. Sci. 16, 1028–1063.

Ali Hussein, A.A., Zhao, L., Chen, Y., Wang, J., 2023. Rock physics characteristics of marine sediments in the South China Sea: the link between the geological factors and elastic properties. Front. Earth Sci. 10.

Ali, M., Jha, N.K., Pal, N., Keshavarz, A., Hoteit, H., Sarmadivaleh, M., 2022. Recent advances in carbon dioxide geological storage, experimental procedures, influencing parameters, and future outlook. Earth Sci. Rev. 225, 103895.

Almenningen, S., Gauteplass, J., Fotland, P., Aastveit, G.L., Barth, T., Ersland, G., 2018. Visualization of hydrate formation during CO2 storage in water-saturated sandstone. Int. J. Greenh. Gas Control 79, 272–278.

Aminnaji, M., Qureshi, M.F., Dashti, H., Hase, A., Mosalanejad, A., Jahanbakhsh, A., Babaei, M., Amiri, A., Maroto-Valer, M., 2024. CO2 gas hydrate for carbon capture and storage applications – part 2. Energy 300, 131580.
Bhati, A., Hamalian, M., Bahadur, V., 2025. Techno-economic modeling of carbon dioxide hydrate formation for carbon sequestration. Appl. Energy 377, 124491.
Bistline, J.E.T., Blanford, G.J., 2021. Impact of carbon dioxide removal technologies on deep decarbonization of the electric power sector. Nat. Commun. 12, 3732.
Bui, M., Adjiman, C.S., Bardow, A., Anthony, E.J., Boston, A., Brown, S., Fennell, P.S., Fuss, S., Galindo, A., Hackett, L.A., Hallett, J.P., Herzog, H.J., Jackson, G., Kemper, J., Krevor, S., Maitland, G.C., Matuszewski, M., Metcalfe, I.S., Petit, C., Puxty, G., Reimer, J., Reiner, D.M., Rubin, E.S., Scott, S.A., Shah, N., Smit, B., Trusler, J.P.M., Webley, P., Wilcox, J., Mac Dowell, N., 2018. Carbon capture and storage (CCS): the way forward. Energy Environ. Sci. 11, 1062–1176.
Castaneda, J.R., Kahrobaei, S., Aghajanloo, M., Voskov, D., Farajzadeh, R., 2025. Numerical and experimental investigation of impact of CO2 hydrates on rock permeability. Fuel 381, 133708.
Chen, G.-J., Guo, T.-M., 1998. A new approach to gas hydrate modelling. Chem. Eng. J. 71, 145–151.
Chen, H.-N., Sun, Y.-F., Pang, W.-X., Wang, M.-L., Wang, M., Zhong, J.-R., Ren, L.-L., Cao, B.-J., Rao, D., Sun, C.-Y., Chen, G.-J., 2024. Quantitative evaluation of hydrate-based CO2 storage in unsealed marine sediments: viewpoint from the driving force of hydrate formation and CO2-water contact ability. Fuel 376, 132682.
Chen, J., Hopmans, J.W., Grismer, M.E., 1999. Parameter estimation of two-fluid capillary pressure–saturation and permeability functions. Adv. Water Resour. 22, 479–493.
Clarke, M.A., Bishnoi, P.R., 2005. Determination of the intrinsic kinetics of CO2 gas hydrate formation using in situ particle size analysis. Chem. Eng. Sci. 60, 695–709.
Dhamu, V., Qureshi, M.F., Barckholtz, T.A., Mhadeshwar, A.B., Linga, P., 2023. Evaluating liquid CO2 hydrate formation kinetics, morphology, and stability in oceanic sediments on a lab scale using top injection. Chem. Eng. J. 478, 147200.
Fu, C., Du, Y., Song, W., Sang, S., Pan, Z., Wang, N., 2023. Application of automated mineralogy in petroleum geology and development and CO2 sequestration: a review. Mar. Petrol. Geol. 151, 106206.
Fukumoto, A., Kamada, K., Sato, T., Oyama, H., Torii, H., Kiyono, F., Nagao, J., Temma, N., Narita, H., 2018. Numerical simulation of pore-scale formation of methane hydrate in the sand sediment using the phase-field model. J. Nat. Gas Sci. Eng. 50, 269–281.
Gu, Y., Liu, X., Li, Y., Lu, H., Xu, C., Ren, J., Chen, G., Linga, P., Zhao, J., Yin, Z., 2025. Feasibility analysis of liquid CO2 injection and sequestration as hydrates in South China Sea marine sediments over 100 years. Appl. Energy 380, 125068.
Guo, Y., Li, S., Sun, H., Wu, D., Liu, L., Zhang, N., Qin, X., Lu, C., 2024. Enhancing gas production and CO2 sequestration from marine hydrate reservoirs through optimized CO2 hydrate cap. Energy 303, 131821.
Hofmann, M., Schellnhuber, H.J., 2010. Ocean acidification: a millennial challenge. Energy Environ. Sci. 3, 1883–1896.
Hosseini Zadeh, A., Kim, I., Kim, S., 2023. Characteristics of CO2 hydrate formation and dissociation at different CO2-water ratios in a porous medium. Int. J. Greenh. Gas Control 125, 103883.
Inui, M., Sato, T., Komai, T., Kagemoto, H., 2011. Experiments and numerical simulations of hydrate formation in sand sediment simulating sub-seabed CO_2 storage in the form of gas hydrate. J. MMIJ 127, 194–201.
Kalam, S., Olayiwola, T., Al-Rubaii, M.M., Amaechi, B.I., Jamal, M.S., Awotunde, A.A., 2021. Carbon dioxide sequestration in underground formations: review of experimental, modeling, and field studies. J. Petrol. Explor. Prod. 11, 303–325.
Ke, W., Svartaas, T.M., Chen, D., 2019. A review of gas hydrate nucleation theories and growth models. J. Nat. Gas Sci. Eng. 61, 169–196.
Khandoozi, S., Hazlett, R., Fustic, M., 2023. A critical review of CO2 mineral trapping in sedimentary reservoirs – from theory to application: pertinent parameters, acceleration methods and evaluation workflow. Earth Sci. Rev. 244, 104515.
Krevor, S., de Coninck, H., Gasda, S.E., Ghaleigh, N.S., de Gooyert, V., Hajibeygi, H., Juanes, R., Neufeld, J., Roberts, J.J., Swennenhuis, F., 2023. Subsurface carbon dioxide and hydrogen storage for a sustainable energy future. Nat. Rev. Earth Environ. 4, 102–118.
Li, M.-y., Gao, M., Zuo, Q.-r., Zhao, Y.-g., Zhang, L.-x., 2022a. Experimental and theoretical investigation on hydrate nucleation in TBAB droplets. Fuel 308, 121994.
Li, M., Fan, S., Wang, Y., Lang, X., Cheng, P., 2024. Heterogeneous nucleation of CO2 hydrate: a thermodynamics analysis considering effects of wall characteristics and solution activity. Int. J. Heat Mass Tran. 224, 125285.
Li, M., Fan, S., Wang, Y., Lang, X., Li, G., 2023a. Effect of surface roughness on methane hydrate formation and its implications in nucleation design. AIChE J. 69, e18069.
Li, M., Fan, S., Wang, Y., Lang, X., Li, G., Wang, S., Yu, C., 2022b. Effect of surface curvature and wettability on nucleation of methane hydrate. AIChE J. 68, e17823.
Li, Q., Han, Y., Liu, X., Ansari, U., Cheng, Y., Yan, C., 2022c. Hydrate as a by-product in CO2 leakage during the long-term sub-seabed sequestration and its role in preventing further leakage. Environ. Sci. Pollut. Control Ser. 29, 77737–77754.
Li, Y., Yang, Y., Dong, M., Yao, J., Zhang, K., Sun, H., Zhang, L., 2023b. In-Situ imaging of CO2 trapping and oil recovery in three-phase systems: dependence on pore geometry and wettability. SPE J. 28, 768–782.
Liu, Y., Qi, H., Liang, H., Yang, L., Lv, X., Qiao, F., Wang, J., Liu, Y., Li, Q., Zhao, J., 2024a. Influence mechanism of interfacial organic matter and salt system on carbon dioxide hydrate nucleation in porous media. Energy 290, 130179.
Liu, Y., Xu, H., Sun, L., Ma, X., Li, H., Jiang, L., Zheng, J.-n., Song, Y., 2024b. CO2 hydrate formation characteristics inside seawater residual/saturated sediments under marine CO2 storage scenes. Energy 309, 132991.
Liu, Z., Xu, J., Li, H., Li, S., Fan, X., 2023. Numerical investigation of CO2 storage capacity via hydrate in deep-sea sediments. Energy Fuels.
Masuda, Y., Fujinaga, Y., Naganawa, S., Fujita, K., Sato, K., Hayashi, Y., 1999. Modeling and experimental studies on dissociation of methane gas hydrates in berea sandstone cores. 3rd International Conference on Gas Hydrates, pp. 18–22.
Matter, J.M., Stute, M., Snæbjörnsdottir, S.Ó., Oelkers, E.H., Gislason, S.R., Aradottir, E. S., Sigfusson, B., Gunnarsson, I., Sigurdardottir, H., Gunnlaugsson, E., Axelsson, G., Alfredsson, H.A., Wolff-Boenisch, D., Mesfin, K., Taya, D.F.d.l.R., Hall, J., Dideriksen, K., Broecker, W.S., 2016. Rapid carbon mineralization for permanent disposal of anthropogenic carbon dioxide emissions. Science 352, 1312–1314.
Nakashima, T., Sato, T., 2016. Numerical modelling of CO2 gas injection with hydrate formation: a case study in the laboratory-scale sand sediment. In: Vishal, V., Singh, T.N. (Eds.), Geologic Carbon Sequestration: Understanding Reservoir Behavior. Springer International Publishing, Cham, pp. 285–300.
Qanbari, F., Pooladi-Darvish, M., Hamed Tabatabaie, S., Gerami, S., 2011. Storage of CO2 as hydrate beneath the ocean floor. Energy Proc. 4, 3997–4004.
Sambo, C., Gupta, I., 2025. Numerical simulation for subsidence control in CO2 storage and methane hydrate extraction. Mar. Petrol. Geol. 171, 107160.
Sawano, Y., Wako, T., Sato, T., Tada, K., 2022. Numerical simulation of the effect of gas hydrate formation on liquid-CO2 leakage suppression in sub-seabed sand sediment. Int. J. Greenh. Gas Control 119, 103728.
Schrag, D.P., 2009. Storage of carbon dioxide in offshore sediments. Science 325, 1658–1659.
Sloan, E.D., 2003. Fundamental principles and applications of natural gas hydrates. Nature 426, 353–359.
Snæbjörnsdóttir, S.Ó., Sigfússon, B., Marieni, C., Goldberg, D., Gislason, S.R., Oelkers, E. H., 2020. Carbon dioxide storage through mineral carbonation. Nat. Rev. Earth Environ. 1, 90–102.
Sun, H., Chen, J., Ji, X., Karunakaran, G., Chen, B., Ranjith, P.G., Song, Y., Yang, M., 2024a. Optimizing CO2 hydrate storage: dynamics and stability of hydrate caps in submarine sediments. Appl. Energy 376, 124309.
Sun, N., Li, Y., Qiu, N., Liu, Z., Francisco, J.S., Du, S., 2024b. Adsorption behaviors for clathrate hydrates of CO2 with mixed gases. Fuel 358, 130265.
Sun, Z.-F., Li, N., Jia, S., Cui, J.-L., Yuan, Q., Sun, C.-Y., Chen, G.-J., 2019. A novel method to enhance methane hydrate exploitation efficiency via forming impermeable overlying CO2 hydrate cap. Appl. Energy 240, 842–850.
Teng, Y., Zhang, D., 2018. Long-term viability of carbon sequestration in deep-sea sediments. Sci. Adv. 4, eaao6588.
Tyne, R.L., Barry, P.H., Lawson, M., Byrne, D.J., Warr, O., Xie, H., Hillegonds, D.J., Formolo, M., Summers, Z.M., Skinner, B., Eiler, J.M., Ballentine, C.J., 2021. Rapid microbial methanogenesis during CO2 storage in hydrocarbon reservoirs. Nature 600, 670–674.
Wang, F., Shen, K., Zhang, Z., Zhang, D., Wang, Z., Wang, Z., 2023. Numerical simulation of natural gas hydrate development with radial horizontal wells based on thermo-hydro-chemistry coupling. Energy 272, 127098.
Wei, R., Xia, Y., Wang, Z., Li, Q., Lv, X., Leng, S., Zhang, L., Zhang, Y., Xiao, B., Yang, S., Yang, L., Zhao, J., Song, Y., 2022. Long-term numerical simulation of a joint production of gas hydrate and underlying shallow gas through dual horizontal wells in the South China Sea. Appl. Energy 320, 119235.
Wei, Y., Nobuo, M., 2023. Nucleation curves of carbon dioxide hydrate in the absence of a solid wall. Energy Fuels 37, 3760–3774.
Xia, Y., Gao, P., Jiang, Z., Fan, Q., Wei, R., Li, Q., Zhang, L., Yu, T., Zhao, J., Yang, L., Song, Y., 2024. Numerical simulation of CO2 storage in subseabed sediments in the shenhu area, South China Sea: the effect of reservoir permeability anisotropy. Energy Fuels.
Xia, Y., Yu, T., Yang, L., Chen, B., Jiang, L., Yang, M., Song, Y., 2025. Multi-state CO2 distribution patterns for subsea carbon sequestration assisted by large-scale CO2 hydrate caps. Energy 320, 135231.
Yamada, K., Fernandes, B.R.B., Kalamkar, A., Jeon, J., Delshad, M., Farajzadeh, R., Sepehrnoori, K., 2024. Development of a hydrate risk assessment tool based on machine learning for CO2 storage in depleted gas reservoirs. Fuel 357, 129670.
Yang, M., Wu, M., Yang, Z., Wang, P., Chen, B., Song, Y., 2024. Behaviors of hydrate cap formation via CO2-H2O collaborative injection:applying to secure marine carbon storage. Gas Sci. Eng. 131, 205451.
Yu, S., Uchida, S., 2020. Geomechanical effects of carbon sequestration as CO2 hydrates and CO2-N2 hydrates on host submarine sediments. E3S Web Conf. 205.
Yu, T., Sato, T., Nakashima, T., Inui, M., Oyama, H., 2016. An integrated model for CO2 hydrate formation in sand sediments for sub-seabed CO2 storage. Int. J. Greenh. Gas Control 52, 250–269.
Yu, Y.-S., Zhang, X., Liu, J.-W., Lee, Y., Li, X.-S., 2021. Natural gas hydrate resources and hydrate technologies: a review and analysis of the associated energy and global warming challenges. Energy Environ. Sci. 14, 5611–5668.
Yuhara, D., Barnes, B.C., Suh, D., Knott, B.C., Beckham, G.T., Yasuoka, K., Wu, D.T., Sum, A.K., 2015. Nucleation rate analysis of methane hydrate from molecular dynamics simulations. Faraday Discuss. 179, 463–474.
Zhang, S., Ma, Y., Xu, Z., Zhang, Y., Liu, X., Zhong, X., Tu, G., Chen, C., 2024. Numerical simulation study of natural gas hydrate extraction by depressurization combined with CO2 replacement. Energy 303, 131998.
Zhao, G., Zheng, J.-n., Gong, G., Chen, B., Yang, M., Song, Y., 2023. Formation characteristics and leakage termination effects of CO2 hydrate cap in case of geological sequestration leakage. Appl. Energy 351, 121896.
Zhao, J., Zheng, J., Ren, L., Lin, R., Zhou, B., 2024. A review on geological storage of marine carbon dioxide: challenges and prospects. Mar. Petrol. Geol. 163, 106757.